

Tracing magnetic field in super-Alfvénic turbulence with Gradient Technique

KA WAI HO^{1,2} AND A. LAZARIAN²

¹*Theoretical Division, Los Alamos National Laboratory*

²*Department of Astronomy, University of Wisconsin-Madison, Madison, WI, 53706, USA*

ABSTRACT

Super-Alfvénic turbulence is important for many astrophysical objects, particularly galaxy clusters. In this paper, we explore the accuracy of Synchrotron Intensity Gradients (SIGs) and X-ray intensity gradients to map magnetic fields in super-Alfvénic turbulence for a set of astrophysically relevant parameters of turbulent driving. Analyzing our synthetic observations, we report a good accuracy for both techniques. Our results are suggestive that other types of Gradient Technique (GT) can be successfully employed to trace magnetic fields within super-Alfvénic sub-sonic turbulence.

Keywords: ISM: structure; ISM: atoms; ISM: clouds; ISM: magnetic fields

1. INTRODUCTION

Magnetic fields and turbulence are ubiquitous in astrophysical settings. MHD turbulence plays an important role on various scales, from millions of parsecs for intracluster medium (ICM) to hundreds of parsecs in the interstellar medium and parsecs, parsecs and astronomical units for star formation, and hundreds of kilometers for stellar winds. The magnetization of the media is extremely important for understanding key astrophysical problems, e.g., the problem of star formation (McKee & Ostriker 2007; Mac Low & Klessen 2004) and cosmic ray propagation and acceleration. (Jokipii 1966; Yan & Lazarian 2008).

Studies of astrophysical magnetic fields are challenging. All magnetic measurements rely on the effects of the magnetic field on the media. The Zeeman technique is the most direct way of measuring the strength of the line-of-sight component of the magnetic field that relies on splitting atomic levels (Crutcher et al. (2010) and ref. therein). However, it is a very challenging approach regarding data requirements and observational time. Measuring synchrotron polarization relies on the interaction of relativistic electrons with the magnetic field Beck et al. (1996). The resulting polarization is perpendicular to the magnetic field. Faraday rotation can affect the synchrotron polarization, which complicates the interpretation of the signal. In addition, Faraday depolarization decreases the polarization signal, especially at low frequencies (Lazarian & Pogosyan 2016). At the same time,

the Faraday rotation from point sources, e.g., pulsars, can be used to probe the strength of the parallel to the line of light magnetic field component in ionized media (see Gaensler et al. (2005)). The measurements are contaminated, however, by the poorly constrained variation of the thermal electron density. Similarly to synchrotron emission, dust particles get aligned with long axes perpendicular to the magnetic field due to the action of radiative torques (RATs) (Lazarian & Hoang 2007) and produce far-infrared emission polarization perpendicular to the magnetic field, while the polarization of starlight resulting from such an alignment is parallel to the magnetic field direction (Andersson et al. (2015) and ref. therein). This approach is applicable to dense media with sufficient dust density and it heavily relies on the alignment properties of dust that vary in space depending on the grain illumination, grain size distribution, and grain disruption (Hoang 2019; Lazarian & Hoang 2021; Tram & Hoang 2022). Additional techniques rely on the polarization that arises from Goldreich-Kylafis effect (Goldreich & Kylafis 1981; Crutcher et al. 2010) and atomic alignment (Yan & Lazarian 2006, 2010; Zhang et al. 2020). Their applications have been limited so far.

All techniques above employ polarization. However, it is known that high-precision polarization measurement is challenging and requires significantly more effort than measurements of signal intensities. As a result, the introduction of a new technique, namely, the Gradient Technique (GT), which may get the magnetic field information without polarization measurements, opens a new avenue for studying astrophysi-

cal magnetic fields in diffuse media.¹ The GT employs the properties of magnetic turbulence. In this paper, our primary goal is to explore the properties of *Synchrotron Intensity Gradients (SIGs)* (Lazarian et al. 2017) that employ gradients of synchrotron intensities. However, our results apply to other incarnations of the GT, e.g., to *Velocity Gradient Technique (VGT)* with its subdivision of Velocity Centroid Gradients (VCGs) that employ Velocity Centroids (González-Casanova & Lazarian 2017; Yuen & Lazarian 2017) and Velocity Channel Gradients (VChGs) (Lazarian & Yuen 2018b) that employ intensity fluctuations in thin channel maps. For subsonic turbulence, density fluctuations arising as entropy fluctuations mimic velocity fluctuations (Davidson 2015).

Therefore, the density gradients can be used as proxies of velocity gradients (Hu et al. 2019). Keeping in mind the application of the technique to diffuse media in galaxy clusters, i.e., Intra Cluster Media (ICM), we study the application of Intensity Gradients (IGs) to X-ray emissivity of turbulent medium.

The GT has been successfully applied to galactic and extragalactic environments with the magnetic maps obtained with the GT successfully compared to those obtained with polarization (Hu et al. 2019, 2021, 2022, 2024). It was also applied to intergalactic media with GT results compared with the magnetic field structure obtained with numerical simulations of galaxy cluster formation (Hu et al. 2020a). The latter case presents is of special interest as the turbulence in galaxy clusters is super-Alfvénic, i.e. has the Alfvén Mach number $M_A = V_L/V_A > 1$, where V_L represents the injection velocity. At the same time, most numerical testing of GT was performed for $M_A \leq 1$.

The present study aims to explore the GT's ability to map magnetic fields in environments corresponding to $M_A > 1$ and $M_A \gg 1$. This study's primary astrophysical application is related to justifying magnetic field studies with the GT in the ICM, but it is also applicable to other branches of the GT.

Below, this paper will utilize the numerical simulation to study the anisotropy statistics of the super-Alfvénic fluid on both small and large scales. Furthermore, we will explore the application of magnetic field tracing with the gradient technique. In what follows we structure our paper in the following way. Section 2 will cover the theoretical considerations behind the GT approach to mapping magnetic fields. In section 3, we will cover the detail of the numerical method. In contrast, in section 4.2, we will discuss the application of synchrotron intensity gradients (SIGs) to super-Alfvénic turbulence and provide a comparison with the sub-Alfvénic case. Section 5 is devoted to effects noise and compress-

ibility. It also illustrates the capabilities of GT in magnetic field tracing with X-ray data. In Section 6, we will discuss the applicability of the results and further research directions. Section 7 will summarize the results of the paper.

2. THEORETICAL CONSIDERATION

2.1. sub-Alfvénic Turbulence and GT

The level of turbulence controls the magnetic field structure and properties of magnetic turbulence. For sub-Alfvénic and trans-Alfvénic turbulence, the observational line-of-sight averaged gradients are dominated by the dominated by Alfvénic modes.

The Alfvénic Mach Number M_A can quantify the magnetization level. Depending on different astrophysical objects, M_A varies from the sub-Alfvénic regime, i.e., $M_A < 1$ the super-Alfvénic regime, i.e., $M_A > 1$ with the special regime of trans-Alfvénic, i.e., $M_A = 1$ regime in between. The hot phase of the interstellar medium (ISM) (see Draine (2006) for a list of the idealized ISM phases) $M_A < 1$. The turbulence may be both sub-Alfvénic and super-Alfvénic in molecular clouds and super-Alfvénic in an intracluster medium (ICM). Graphically, the level of magnetization is associated with the topology of the field lines is shown in Figure 1. The streamlines represent the B-field direction. The left panel of the figure depicts B-field lines with only minor variations in the sub-Alfvénic regime. In contrast, the right panel of Figure 1 shows a highly disorganized magnetic field in the super-Alfvénic case. Naturally, the difference in magnetic field structure can entail the difference in the properties of gradients. Thus, below, we briefly explain what is known about the magnetic field properties in sub-Alfvénic and super-Alfvénic regimes.

The magnetization level could also shape the local fluctuation on other physical quantities and can be used to trace the B-field lines. Modern Theory of MHD turbulence (see Beresnyak & Lazarian (2019)) suggests that for $M_A \leq 1$ a scale-dependent anisotropic cascade exists of Alfvénic modes. This cascades shapes the cascade of slow modes while leaving fast MHD modes marginally affected (Goldreich & Sridhar (1995); Lazarian & Vishniac (1999), GS95 and LV99, respectively, Cho & Lazarian (2002, 2003); Lithwick & Goldreich (2001)). For Alfvén and slow modes, the eddies are elongated along mean field lines, and the elongation increases at a small scale. The GT, when applied to sub-Alfvénic turbulence, utilizes this anisotropy to trace the magnetic field. The physics of this tracing is obvious from the picture of magnetic eddies aligned with the magnetic field that follows from the theory of turbulent reconnection in LV99. Indeed, LV99 predicts that the time scale for turbulent reconnection equals the eddy turnover time. Therefore, the eddies that mix magnetized fluid in the direction perpendicular *local* magnetic field that surrounds the eddies are not subject to the magnetic field back-reaction. This provides the natural direction of least resistance along which the turbulent energy cascades. As the eddies mix the magnetized fluid, the Alfvénic perturbations are induced within a period equal to

¹ Note that GT can also employ polarization to get extra information about the magnetic field. For instance, as shown in Lazarian & Yuen (2018a), Synchrotron Polarization Gradients (SPGs) can use synchrotron polarization at different wavelengths to probe magnetic fields at different distances along the line of sight (Ho et al. 2019; Zhang et al. 2019, 2020), while Faraday Gradients (FGs) can get the distribution of plane of sky direction of the magnetic field. However, we do not discuss polarization versions in the present paper.

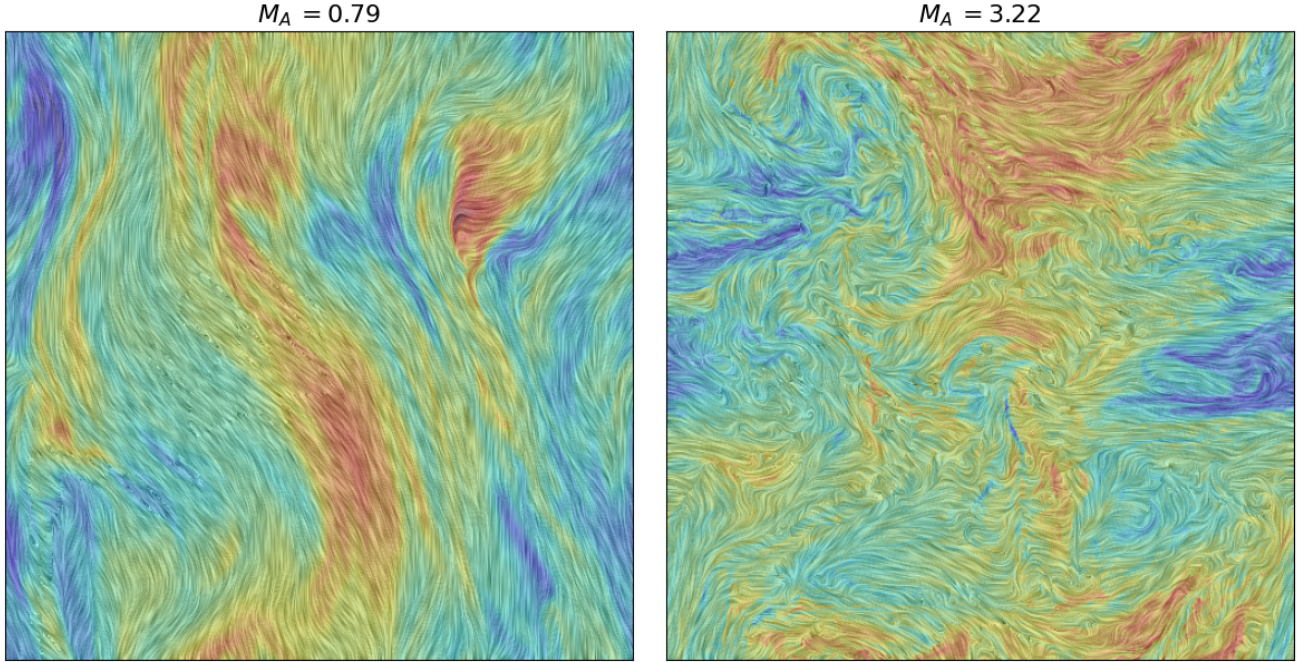


Figure 1. Intensity of projected velocity fluctuation (color plot) overlaid with projected magnetic field lines (streamline plot).

the eddy turnover time. Equating the two values, one gets

$$l_{\perp}/v_l = l_{\parallel}/V_A, \quad (1)$$

where l_{\parallel} is the eddy extent parallel to the local direction of the magnetic field, while l_{\perp} is the eddy extent perpendicular to the local magnetic field. It was shown in LV99 that for $M_A \leq 1$ Eq. (1) entails the relation between the parallel and perpendicular eddy sizes

$$l_{\parallel} \approx L \left(\frac{l_{\perp}}{L} \right)^{2/3} M_A^{-4/3}, \quad (2)$$

where L is the injection scale of turbulence. Eq. (2) testifies that the eddies get more and more elongated along the local directions of the magnetic field as the eddy size decreases. Thus, at a sufficiently small scale, eddies act as compass needles aligned with the nearby magnetic fields. Naturally, the gradients of both velocities and magnetic fields arising from such eddies are perpendicular to the local magnetic field. In other words, the velocity and magnetic field gradients can act similarly to dust grains aligned by the magnetic field and trace the field direction.

Eq. (1) is known as *critical balance*. This concept was introduced in the pioneering MHD turbulence study in GS95. However, as a note of caution, we should mention that in GS95, the critical balance is formulated in Fourier space with the parallel to magnetic field axis aligned with the mean magnetic field. Similarly, for $M_A = 1$, GS95 formulated the relation for the scale-dependent anisotropy $k_{\parallel} \sim k_{\perp}^{2/3}$ in the mean magnetic field system of reference. The corresponding confusion in relation to the system of references still exists in the literature, although the fact that the Alfvénic turbulence scaling is only valid in the system of reference was

confirmed by numerical simulations (Cho & Vishniac 2000; Maron & Goldreich 2001) and is the basis of the further theoretical studies (Yan & Lazarian 2002; Farmer & Goldreich 2004). The notion of *local* system of reference is absolutely fundamental for the GT.

For $M_A \leq 1$, Eq. (1) is satisfied for scales smaller than the scale (see LV99)

$$l_{trans} \approx LM_A^2. \quad (3)$$

For scales in the range $l_{trans} < l < L$, the turbulence isotropically injected at scale L is in the weak regime, in which the cascade induces the decrease of l_{\perp} which keeps the parallel scale of turbulent fluctuations unchanged (LV99, Galtier et al. (2000)). As a result, in both regimes the gradients are perpendicular to the magnetic field direction and GT can trace magnetic field.

For $M_A \leq 1$ the scaling of turbulent velocity motions at $l < l_{tran}$ (LV99)

$$v_l \approx V_L \left(\frac{l_{\perp}}{L} \right)^{1/3} M_A^{1/3}, \quad (4)$$

i.e., Kolmogorov if the velocity is measured as a function of scale l_{\perp} , i.e., $v_l \sim l_{\perp}^{1/3}$. Naturally, the same type of scaling, i.e., $b_l \sim l_{\perp}^{1/3}$, is expected for Alfvénic turbulent fluctuations. As we mentioned earlier, the slow modes are slaved by Alfvén modes and copy the Alfvén mode scaling. As a result, both for Alfvén and slow modes, the gradients scale as

$$v_l/l_{\perp} \sim b_l/l_{\perp} \sim l_{\perp}^{-2/3} \quad (5)$$

i.e., the turbulent motions at the smallest scales induce the largest amplitude gradients. Together with the fact that the

gradients are closely aligned with *local* magnetic field, this enables mapping of projected magnetic fields.

2.2. super-Alfvénic turbulence and GT

The turbulence is different for super-Alfvénic and sub-Alfvénic cases. This can be seen from Figure 1, which shows the synthetic observations of magnetic field lines in turbulence corresponding to $M_A < 1$ (left panel) and $M_A > 1$ (right panel).

It is obvious that if $M_A \gg 1$, most of the turbulent energy is in the form of hydrodynamic motions. For our purposes, the action of the non-linear turbulent dynamo can be disregarded as it transfers only 3/38 fraction of the energy cascade into the magnetic field (Xu & Lazarian 2016). Therefore, in the weakly compressible limit, i.e., for low sonic Mach number, $M_s = V_L/V_s$, where V_s is the sound velocity, we expect to have the Kolmogorov cascade for supersonic turbulence at the injection scale.

In Kolmogorov turbulence, turbulent motions scale as $v_l \sim (l/L)^{1/3}$. Thus, the kinetic energy of turbulent eddies decreases as $(l/L)^{2/3}$ with the decrease of the scale l . As a result for turbulence with $M_A > 1$ at the transition scale (Lazarian 2006)

$$l_A = LM_A^{-3} \quad (6)$$

the turbulent velocity gets equal to the Alfvén velocity V_A .

Therefore, one can roughly subdivide the range of turbulent scales into two regions: Kolmogorov turbulence for $l_{tr} < l < L$ and the MHD trans-Alfvénic turbulence for $l < l_{tr}$. For the first regime where at these large scales ($l > l_A$), the turbulence is isotropic, magnetic fields are passively moved by strong hydrodynamic motions. For the second regime, magnetic fields are dynamically important and determine the evolution of the cascade (Goldreich & Sridhar 1995; Kraichnan 1965). One can expect that the GT will act differently for these two regimes.

2.3. Gradients and Plane of Sky Magnetic Field Direction

The measurements of 3D magnetic fields with gradients are rarely available. As a rule, one gets the measurements that include both line-of-sight averaging and telescope beam averaging. Due to the latter effect, the smallest scale at which the gradients can be measured is determined by the telescope resolution l_{res} . Therefore, according to Eq. (5), the GT samples magnetic field structure at scales larger than l_{res} .

The averaging along the line of sight further modifies the gradient statistics. The gradient measured from the 2D observation maps can be considered the proxy of the 3D fluctuation (Lazarian et al. 2017). Gradients are measured for turbulent volume extended by $\mathcal{L} > L_{inj}$ along the LOS, and this entails additional complications, where \mathcal{L}, L_{inj} is the LOS depth and the injection scale. While eddies stay aligned with the local magnetic field, the direction of the local magnetic field is expected to change along the LOS. Thus, the contribution of the 3D velocity gradient is also summed up along the line of sight.

The summation of gradients, however, is different for sub-Alfvénic and super-Alfvénic cases. The contributions of gra-

dients at the scale l_{res} are being summed up along the line of sight. For $M_A < 1$ and line of sight perpendicular to the mean magnetic field, the gradients add up along the line of sight, reflecting the structure of the averaged magnetic field along the line of sight. The same structure is being sampled by velocity and magnetic field gradients due to Eq. (5).

For $M_A > 1$, consider first velocity gradients. If the scale $l_{res} < l_A$, the contributions from regions of the size l_A are summed up along the line of sight. These contributions aligned with the mean magnetic field in independent magnetic domains of size l_A . The latter is randomly oriented; thus, the summation is happening in a random walk manner. This increases the role of the gradients arising from the large-scale motions of the largest eddies $\sim L$. Finally, for $l_{res} \gg l_A$, the velocity gradients sample only hydrodynamic eddies. The contributions from the gradients arising from eddies at the scale l_{res} are completely random and cancel out due to line-of-sight averaging.

The magnetic field for $M_A \gg 1$ is passively advected by velocity motions on the scales much larger than l_{res} . Therefore, the magnetic fields are aligned with the flow lines of the large-scale eddies. The velocity gradients are perpendicular to the flow lines in solenoidal hydrodynamic turbulence. This results in the observed velocity gradients being perpendicular to the magnetic fields in large-scale eddies. As for $M_A \gg 1$, magnetic field lines follow the velocity flow lines; the magnetic field gradients are also perpendicular to the direction of the large-scale magnetic field.

In the present study, we will analyze velocities obtained with velocity centroids and magnetic fields represented by synchrotron intensities. A limited study of synchrotron gradients for $M_A > 1$ is presented in Lazarian et al. (2017), but here we provide an extensive parameter study of this regime. We also note that this study only considers the case of magnetic fields in driven turbulence, and the results may differ in more complex astrophysical environments.

3. NUMERICAL METHOD

Motivated by studies of magnetic fields in the ICM medium, we focus on weakly compressible media corresponding to small sonic $M_s = V_L/V_s$, where V_s is the sound velocity and high Alfvén Mach M_A numbers. Therefore, we employ super-Alfvénic incompressible simulations formally corresponding to $M_s = 0$. To explore the effects of compressibility, however, we compare our results with super-Alfvénic compressible simulations with $M_s \sim 1$.

The set of simulations is chosen so that for the low Alfvén Mach number $M_A \sim 2$, the Alfvénic scale l_A (see Eq. 6) is resolved, while for the largest Alfvén Mach number $M_A \sim 5$, the entire simulation corresponds to super-Alfvénic regime, i.e. l_A is less than the scale of numerical dissipation (see table 1, and table 2)

3.1. Super-Alfvénic Incompressible Simulations

The grid-based method (e.g., Finite Volume/Difference) often introduces artificial viscosity, marking the fluid to enter the dissipation regime soon and hard to study the anisotropy

Simulation	M_A	N^3	μ or η	$l_A/\Delta x$
M1	2.4			37.0
M2	2.9	512^3	5×10^{-5}	21.0
M3	3.2			15.6
M4	5.2			3.64
M5	7.8			1.07

Table 1. Key parameters of the MHD incompressible simulation that are used in this paper. M_A , μ/η , N^3 refer to the Alfvénic Mach Number, kinetic/magnetic diffusivity, and resolution of the simulation. The term " $l_A/\Delta x$ " refers to the ratio between the transition scale and the pixel resolution. When $l_A/\Delta x \gg 1$, it indicates that the simulation is in a well-resolved regime, while if $l_A/\Delta x$ is close to 1, it means that the simulation is in a barely resolved regime.

statistics of MHD turbulence in a small scale. So, we use the pseudo-spectral method to simulate super-Alfvén fluid in this paper. The simulations were performed using the pseudo-spectral code `MHDFlows.jl` (Ho 2022)². `MHDFlows.jl` is the newly developed MHD code based on the dynamical language Julia with `FourierFlows.jl` (Constantinou et al. 2023) framework. In contrast to the traditional spectral solver, it supports native GPU acceleration. In our paper, we solve the ideal incompressible MHD equation in the periodic box with the size of 2π :

$$\begin{aligned} \frac{\partial \vec{v}}{\partial t} + (\vec{v} \cdot \nabla) \vec{v} &= -\nabla P + (\nabla \times \vec{B}) \times \vec{B} + \nu \nabla^2 \vec{v} \\ \frac{\partial \vec{B}}{\partial t} &= \nabla \times (\vec{v} \times \vec{B}) + \mu \nabla^2 \vec{B} \end{aligned} \quad (7)$$

All the symbols have their usual meaning. Pressure P is chosen such that the equations maintain the divergence-free condition throughout the simulation. For super-Alfvénic fluid in astrophysics, it is often under the sub-sonic regime, meaning that the compressibility of fluid is a weak and incompressible simulation is an adequate choice to study the behavior of the fluid. For each simulation, The turbulence is driven on large scale through the method proposed by Alvelius (1999). In addition, a weak seed field was injected at the beginning of the simulation, and we analyzed the result after three large-scale eddies turnover times. We choose 2 Storage 5 Stages RK4 method (LSRK54) (see Carpenter & Kennedy (1994) for theory and Fletcher (2015) for actual Implementation) for the time integration and 2/3 alias rule. Table 1 shows the key parameter of the simulation.

3.2. super-Alfvénic Compressible Simulation

To gain insight into the impact of compressibility on the results, we include two super-Alfvénic trans-sonic simulations

Simulation	M_S	M_A	Resolution	$l_A/\Delta x$
A1	1.04	2.3	512^3	42.1
A2	1.02	4.8		4.62

Table 2. Key parameters of the Athena++ simulation that are used in this paper.

in our paper. We employ the 3D MHD simulations generated from the Athena++ MHD code (Stone et al. 2020) to set up a 3D, uniform, and isothermal turbulent medium. The simulations are set up with periodic boundary conditions with solenoidal turbulence injections.

In order to retain the small-scale spatial information required for the GT, we select the 4th order reconstruction method from Athena++. After two large-scale eddy turnover times, a snapshot of the simulation is analyzed. Table 2 shows the key parameter of the simulation.

4. SYNCHROTRON INTENSITY GRADIENTS

4.1. SIGs for super-Alfvénic turbulence

For the power-law distribution of electrons $N(E)E \sim E^\alpha dE$, the synchrotron emissivity is

$$I_{sync}(\mathbf{X}) \propto \int dz B_{POS}^\gamma(\mathbf{X}, \mathbf{z}) \quad (8)$$

where $B_{POS}^\gamma = \sqrt{B_x^2 + B_y^2}$ corresponds to the magnetic field component perpendicular to the line of sight, \mathbf{X} is the plane of sky vector defined in x and y direction, z the line of sight axis and, B_x, B_y the 3D magnetic field in x and y direction. We consider that the variations of cosmic ray density n_{cr} occur on scales larger than those of the magnetic field variations, so that the synchrotron intensity depends only on the magnetic field. The fractional power of the index $\gamma = (\alpha + 1)/2$ was an impediment for quantitative synchrotron statistical studies. As discussed in Lazarian & Pogosyan (2012), the choice of γ varies depending on which physical processes play a role in shaping the spectra, including shock acceleration, turbulence reacceleration, and propagation. These processes lead to a range of γ values, typically between 1 and 4. Lazarian & Pogosyan (2012) showed that the correlation functions and spectra of B_\perp^γ could be expressed as $\alpha = 3$, which gives γ and therefore the dependence of synchrotron intensity on the squared magnetic field strength. We pick $\gamma = 2$ as it is similar to the case of observed cosmic-ray index $\alpha \approx 2.7$. In Lazarian & Pogosyan (2012), the relation between the structure functions obtained for different γ of synchrotron emission and those obtained for $\gamma = 2$ was established.

4.1.1. Gradients

This section will briefly explain the procedure of applying gradients and our analysis.

Due to the statistical nature of turbulence, the individual gradient vector orientation may not represent the local mag-

² <https://github.com/MHDFlows/MHDFlows.jl>

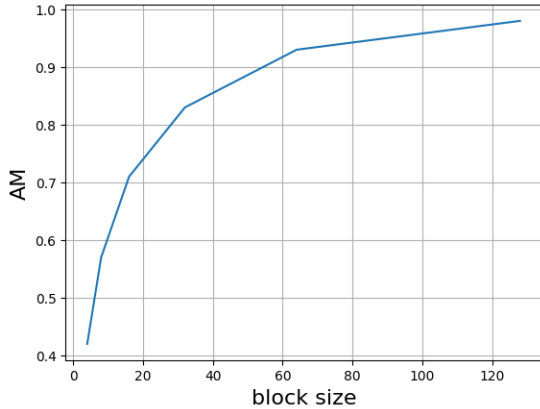


Figure 2. The AM of gradient versus the block size using synchrotron intensity. The simulation used: M1
Block size covered: [4,8,16,32,64,128]

netic field direction. Therefore, one should use the statistical distribution of gradients to trace the magnetic field. The finding converts to the technique called sub-block averaging Yuen & Lazarian (2017).

We divide the observational map into different sub-regions to trace the gradient orientation in a sub-region. For each sub-region, we conduct orientation statistics of gradient vectors and find their best fit of the Gaussian profile, in which the peak of the Gaussian profile reflects the statistical most probable magnetic field orientation in this sub-block. One important note is that as the area of the sampled region increases, the magnetic field’s prediction traced through Gaussian block fit becomes more and more accurate. This means that to increase the accuracy of gradients, we have to sacrifice some of the resolution of the resulting magnetic field maps.

To quantify how good gradients and magnetic fields are aligned, we employ the *alignment measure* AM that is introduced in analogy with the grain alignment studies (see Lazarian 2007):

$$AM = 2\langle \cos^2 \theta_r \rangle - 1, \quad (9)$$

and was discussed for the GT in González-Casanova & Lazarian 2017; Yuen & Lazarian 2017). The range of AM is $[-1, 1]$ measuring the relative alignment between the 90° -rotated gradients and magnetic fields, where θ_r is the relative angle between the two vectors. A perfect alignment gives $AM = 1$, whereas random orientations generate $AM = 0$, and a perfect perpendicular alignment, i.e., “wrong alignment case,” corresponds to $AM = -1$. In what follows, we use AM to quantify the alignments of GT with respect to the magnetic field.

4.2. Magnetic field tracing in super-Alfvénic observations

We construct a synthetic observation for synchrotron intensity (the method described at sec. 3 to study the gradient performance for simulations with Alfvénic Mach number M_A . We apply the sub-block averaging to both gradient and magnetic field vectors to trace the local gradient and magnetic field direction. Similar to studies in Ho & Lazarian

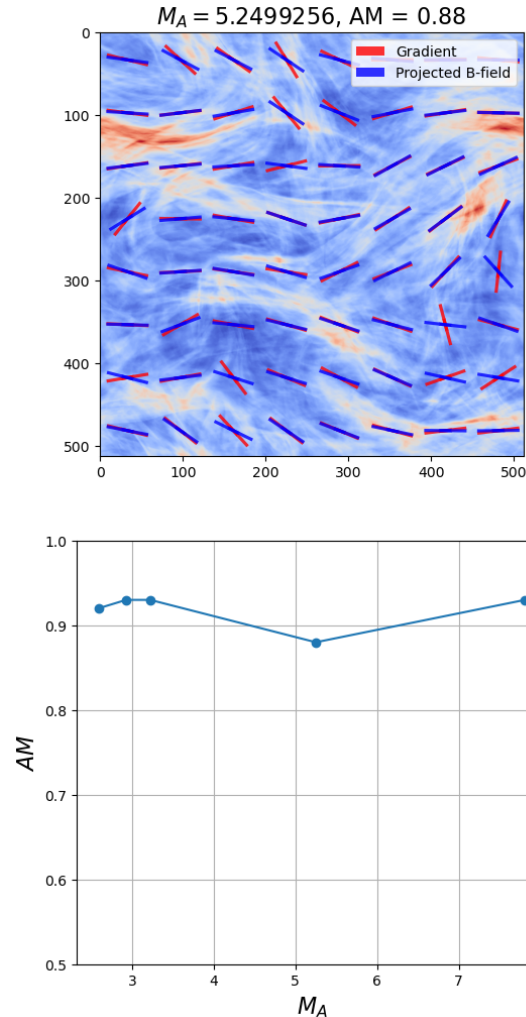


Figure 3. Top panel: synchrotron intensity Map for simulation M4 overlay with gradient and polarization vector. Color with warmer colors represents stronger intensity. Bottom panel: The AM across different M_A .

(2023), the accuracy of the magnetic field tracing is highly related to the choice of block size. The same applies to our super-Alfvénic simulations, and Figure 2 shows the correlation between the two. We use AM to represent the statistical alignment between the gradient and magnetic field directions. The AM increase significantly from 0.4 to 0.93 when the block size is increased from 4^2 to 64^2 . This supports our point that for small averaging, the gradients are unreliable, especially as the size of 4 points is below the numerical dissipation scale of our simulations. For better statistics, we fixed our paper’s block size to 64^2 . Note that our studies are affected by numerical dissipation, and the smaller block sizes can potentially be applied for realistic observations for which the dissipation scale is much smaller than the resolution scale l_{res} .

Below we study the gradient technique in different Alfvénic Mach numbers with the fixed block size 64^2 . The

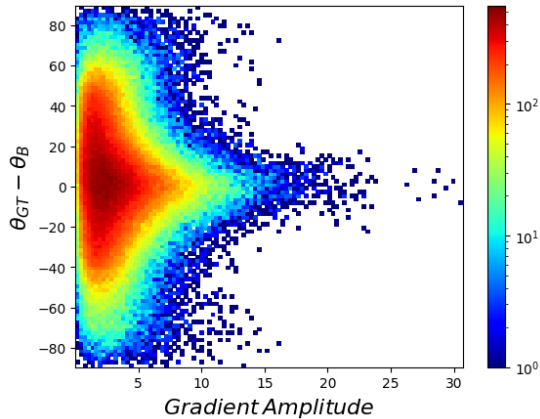


Figure 4. The relative degree - gradient amplitude histogram. Y-axis: the relative degree between individual gradient vector directions. X-axis: the gradient amplitude value. Color bar: log scale pixel count. The simulation used: M4

top panel of Figure 3 shows a graphical result of applying the block averaging method to one of the simulations. The bottom panel shows the AM value for each simulation using the same block-averaging method. One can see from the top panel that, for the most part of the map, the calculated gradient vectors align well with the projected 2D B-field directions (red and blue arrow). It is only a few gradient vectors that are misaligned. As a result, we conclude that statistically the gradient vectors align well with B-field for both sub-Alfvénic and super-Alfvénic simulations. These trends apply to all of our super-Alfvénic simulations with an average $AM \approx 0.9$ (bottom panel, equivalent to $\Delta\theta \sim \pm 10^\circ$). We also note that the alignment only weakly depends on M_A . We note that such similar tendencies are also observed for compressible sub-Alfvénic simulation in Ho & Lazarian (2023)

We also noted from Figure 2 that part of the gradient vectors on the right-hand side diverges from the B-field direction. For regions with poor alignment, we observe that,

1. the amplitude of the plane of the sky magnetic field in those regions has a uniform angular distribution along the line of sight, meaning that the projected magnetic field has low amplitude
2. the gradient amplitude value of those regions tends to be low.

This means that the statistical significance of the magnetic field detection along such directions is low with polarization and gradients. Therefore, the significance of the observed discrepancies between the actual projected magnetic field and that measured with gradients is low. Such points will be within the noise.

To test our hypothesis that in the super-Alfvénic case, the dispersion in angle between the gradient and the projected magnetic field is correlated with the gradient amplitude, we plot in Figure 4, a 2D histogram of relative angle versus gradient amplitude. We see a clear statistical relationship: the

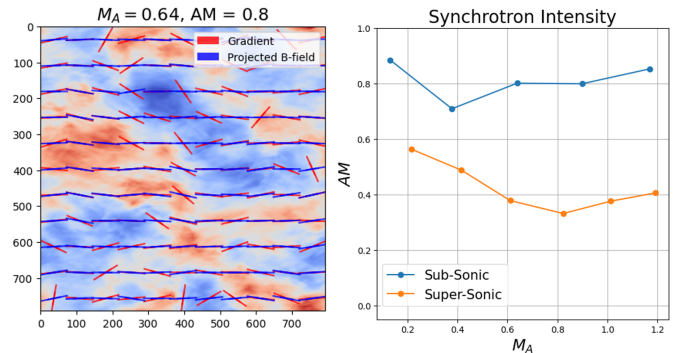


Figure 5. Extracted Figure from (Ho & Lazarian 2023). The left panel shows the result of SIG in a subsonic sub-Alfvénic simulation. The right panel shows the change of AM in difference M_A in both subsonic ($M_S \approx 0.6$) and supersonic ($M_S \approx 6$) regime

pixels with higher gradient amplitude are more aligned with the projected B-field, while the lower amplitude gradients have more dispersion. This finding opens a way of improving the tracing of the magnetic field by filtering out the points corresponding to low amplitudes of gradients. To improve the accuracy of GT magnetic field mapping, we will explore this and other types of filtering elsewhere.

4.3. Comparison: SIGs for sub-Alfvénic turbulence

The regime of sub-Alfvénic turbulence is very different regarding the physics underlying the gradient technique. To have a complete picture of the SIG performance, we present the results for sub-Alfvénic simulations.

SIGs were introduced in Lazarian et al. (2017) and applied to Planck synchrotron emission studies there. The left panel in Figure 5 shows the comparison of predicted directions of obtained with SIGs applied to data of subAlvenic sub-sonic simulations with the maps of the line of sight (LOS) projected magnetic field. The relationship between AM and M_A in sub-Alfvénic simulations is displayed in the right panel of Figure 5. This graph is extracted from the Ho & Lazarian (2023) and includes results from both sub-sonic and super-sonic regimes.

Comparing results in Figure 5 to Figure 3 and Figure 7, we conclude that the alignment is not sensitive to the magnetization and maintaining a good tracing performance.

5. ADDITIONAL EFFECTS

5.1. Synthetic observations: the presence of noise

To test the impact of noise on the tracing performance of the gradient technique, we constructed a synthetic maps incorporating the effect of noise. The results are shown in Figure 6, which demonstrates the dependence of the AM on the noise level.

Three different noise levels were added to the data, ranging from 1σ to 3σ of the map intensity value. The results indicate that AM decreases as the noise level increases. The noise impacts the performance more for small block sizes, which

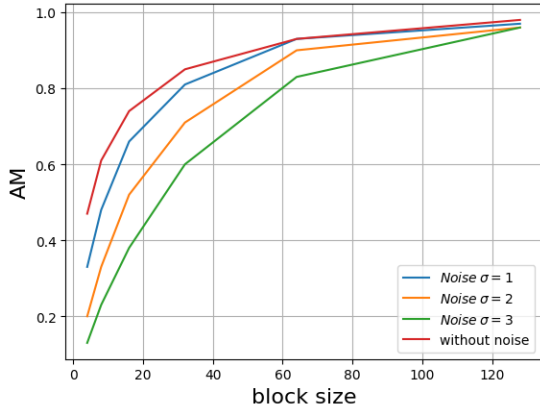


Figure 6. Effect of noise for the gradient technique. Simulation used: M1

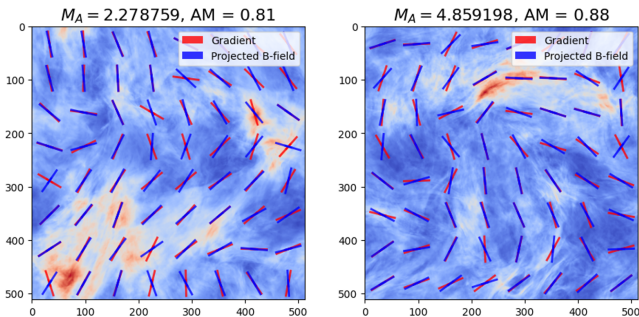


Figure 7. Synchrotron intensity Map overlay with gradient and polarization vector. Simulation used : A1 (Left), A2(Right)

do not have sufficient statistics to start with, while the decline is milder for block sizes greater than 64^2 .

5.2. Effect of compressibility

Incompressible simulations provide a good representation of subsonic turbulence in various astrophysical media, e.g., in the ICM. To gauge the effect of compressibility for the GT, we employ our trans sonic simulations. The setup is described in 4.2.

Figure 7 demonstrates the magnetic field tracing by SIGs for trans-sonic super-Alfvénic turbulence. We see a decrease of AM , but one can see that even for this case, the general structure of the magnetic field can be correctly represented by the GT.

Comparing GT results for trans-sonic super-Alfvénic turbulence in Figure 7 with those in Figure 3) that represent the subsonic super-Alfvénic case, we observe that the decrease of the AM is more noticeable for $M_A \sim 2$ compared to $M_A \sim 5$. The significance of this effect requires further studies, however.

In our sub-Alfvénic studies, we have developed a toolbox to improve the accuracy of GT Ho & Lazarian (2023); Hu & Lazarian (2022). We expect a similar study for super-

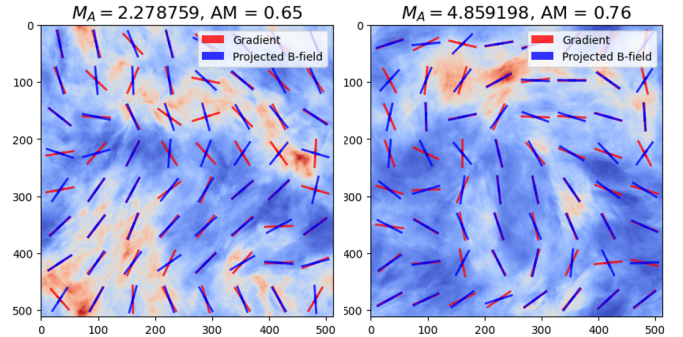


Figure 8. X-ray intensity Map overlay with X-ray gradient and polarization vector. Simulation used : A1 (Left), A2(Right)

Alfvénic GT tracing to improve magnetic field mapping further.

5.3. GT application to X-Ray Intensities

Using X-ray maps, gradients were applied to map the magnetic fields in galaxy clusters (Hu et al. 2020a). The point of whether the accuracy of such mapping depends on resolving the Alfvénic scale l_A given by Eq. (6) was not resolved in Hu et al. (2020a). Below we illustrate the effects of such mapping in settings that both marginally resolved l_A , i.e., corresponding to $M_A \sim 2$, and not resolved l_A , i.e., corresponding to $M_A \sim 5$.

We construct a synthetic X-ray emission map using our Athena++ simulation. The intensity map, I , is defined as follows:

$$I = \int_{LOS} n^2 dx. \quad (10)$$

The result of the intensity gradient compared to the projected magnetic field is shown in Figure 8. We observe that GT can be successfully applied to studying trans-sonic super-Alfvénic turbulence. Compared to Figure 7, we observe a worse X-rays performance than synchrotron, which is expected, as for trans-sonic turbulence, the density statistics do not strictly follow that of velocities. However, the AM observed is significant enough to justify studying magnetic fields in turbulence for the case when l_A is only marginally resolved or not resolved at all.

6. DISCUSSION

Magnetic field tracing in galaxy clusters is a challenge. Observational studies using Faraday rotation showed the magnetic field line of clusters is weak (e.g., Vogt & Enßlin (2003); Bonafede et al. (2010)). Measuring the POS magnetic field component is very difficult (Beck et al. 1996; Eatough et al. 2013; Pakmor et al. 2020) due to the Faraday depolarization of the signal. In this situation, GT presents a unique way to map the magnetic fields in ICM.

While our earlier GT numerical studies mostly dealt with the turbulent medium in the sub-Alfvénic or trans-Alfvénic regime, the clusters of galaxies are in the super-Alfvénic

regime. This deficiency is compensated for in this paper. In Lazarian et al. (2017); Hu et al. (2024), the ability of SIGs to trace magnetic fields in super-Alfvénic turbulence was demonstrated for $M_A \approx 3$. In the current paper, we provide an extensive parameter study for different M_A and prove that the magnetic field good magnetic field tracing is possible for various M_A . We prove that SIGs trace the magnetic field well both when the observations resolve and do not resolve the Alfvén scale l_A . This means we do not have rigid constraints on the required resolution of observations.

The unique property of SIGs is that they are not sensitive to the Faraday depolarization effect, the latter being a serious limitation for present and future synchrotron polarization studies of ICM magnetic fields. Indeed, this depolarization is very strong for low-frequency synchrotron emission. However, the synchrotron emission from most of the ICM, e.g., from cluster halos, is observed at low frequencies only. Thus, SIGs provide a unique way to map magnetic fields in galaxy clusters and recently discovered larger structures, i.e., Megahaloes Knowles et al. (2022). This paper also provides additional support for the magnetic field maps obtained by Hu et al. (2024).

Our work shows that SIGs present a powerful tool for mapping super-Alfvénic magnetic fields in galaxy clusters but are not limited by this. Our previous study in Hu et al. (2020b) argued that the magnetic lines could be traced using the GT applied to X-rays. Applying the GT to X-ray maps was intriguing as it provides a way to utilize these maps for a new purpose, i.e., for magnetic field studies. This opened an avenue for significantly increasing the scientific output of the X-ray galactic cluster observations. However, in the earlier study, the resolution of the scale l_A was assumed to be essential for this tracing. In reality, l_A is not well defined, and thus, the accuracy of magnetic field mapping in Hu et al. (2020b) could be questioned. The removal of the constraint of resolving l_A that we demonstrated provides valuable support with the accuracy of maps obtained with X-ray maps in Hu et al. (2020b).

Our work is also important in a broader context of the advancement of GT technique. It has numerically demonstrated

that the GT can accurately trace magnetic fields in various turbulence regimes, from $M_A < 1$ to $M_A \gg 1$. While our paper only deals on the gradient in the synchrotron and X-ray intensity, the concept of gradient also applies to other data sets, e.g., velocity centroids and velocity channel data. In addition, magnetic field tomography using Synchrotron Polarization Gradients (SPGs) Lazarian & Yuen (2018a) was tested for sub-Alfvénic turbulence. Our present study suggests that the possibility of such a tomographic study can also apply to the super-Alfvénic case. Those results suggested the broad application of G.T. in different astrophysical environment, that may handle handle more complicated conditions, including contact discontinuities where fluid properties and magnetic field jump almost arbitrarily. These applications would be worth to be explored in the future study

7. SUMMARY

In this paper, we numerically studied the applicability of the GT for tracing magnetic field in super-Alfvénic turbulence. Our main results are:

1. Even though the turbulence is large-scale super-Alfvénic and the cascade is hydrodynamic, the GT can successfully trace the magnetic field. This results from dynamically unimportant magnetic fields passively moving by powerful large-scale hydrodynamic eddies.
2. The effects of noise and compressibility do not prevent POS magnetic tracing by the GT. The sub-block averaging procedure works reliably in the super-Alfvénic case.
3. The GT was demonstrated to apply to magnetic field tracing using synchrotron intensities and X-ray maps for conditions similar to those in clusters of galaxies.

ACKNOWLEDGMENTS.

We acknowledge Ka Ho Yuen and Yue Hu for the fruitful discussions. We acknowledge the support the NASA ATP AAH7546 and NASA TCAN 144AAG1967 grants.

Software: Athena++ (Stone et al. 2020), Matplotlib (Hunter 2007), Julia (Bezanson et al. 2017), MHDFlows (Ho 2022)

REFERENCES

- Alvelius, K. 1999, *Physics of Fluids*, 11, 1880, doi: [10.1063/1.870050](https://doi.org/10.1063/1.870050)
- Andersson, B. G., Lazarian, A., & Vaillancourt, J. E. 2015, *ARA&A*, 53, 501, doi: [10.1146/annurev-astro-082214-122414](https://doi.org/10.1146/annurev-astro-082214-122414)
- Beck, R., Brandenburg, A., Moss, D., Shukurov, A., & Sokoloff, D. 1996, *ARA&A*, 34, 155, doi: [10.1146/annurev.astro.34.1.155](https://doi.org/10.1146/annurev.astro.34.1.155)
- Beresnyak, A., & Lazarian, A. 2019, *Turbulence in Magnetohydrodynamics*
- Bezanson, J., Edelman, A., Karpinski, S., & Shah, V. B. 2017, *SIAM review*, 59, 65. <https://doi.org/10.1137/141000671>
- Bonafede, A., Feretti, L., Murgia, M., et al. 2010, *A&A*, 513, A30, doi: [10.1051/0004-6361/200913696](https://doi.org/10.1051/0004-6361/200913696)
- Carpenter, M. H., & Kennedy, C. A. 1994, *Fourth-order 2N-storage Runge–Kutta schemes*, Technical Report NASA TM-109112, NASA Langley Research Center, VA
- Cho, J., & Lazarian, A. 2002, *PhRvL*, 88, 245001, doi: [10.1103/PhysRevLett.88.245001](https://doi.org/10.1103/PhysRevLett.88.245001)
- , 2003, *MNRAS*, 345, 325, doi: [10.1046/j.1365-8711.2003.06941.x](https://doi.org/10.1046/j.1365-8711.2003.06941.x)
- Cho, J., & Vishniac, E. T. 2000, *ApJ*, 539, 273, doi: [10.1086/309213](https://doi.org/10.1086/309213)

- Constantinou, N. C., Wagner, G. L., Palóczy, A., et al. 2023, *FourierFlows/FourierFlows.jl*: v0.10.3, v0.10.3, Zenodo, doi: [10.5281/zenodo.7631539](https://doi.org/10.5281/zenodo.7631539)
- Crutcher, R. M., Hakobian, N., & Troland, T. H. 2010, *MNRAS*, 402, L64, doi: [10.1111/j.1745-3933.2009.00802.x](https://doi.org/10.1111/j.1745-3933.2009.00802.x)
- Davidson, P. A. 2015, *Turbulence: An Introduction for Scientists and Engineers*, 2nd edn. (Oxford University Press)
- Draine, B. T. 2006, *ApJ*, 636, 1114, doi: [10.1086/498130](https://doi.org/10.1086/498130)
- Eatough, R. P., Falcke, H., Karuppusamy, R., et al. 2013, *Nature*, 501, 391, doi: [10.1038/nature12499](https://doi.org/10.1038/nature12499)
- Farmer, A. J., & Goldreich, P. 2004, *ApJ*, 604, 671, doi: [10.1086/382040](https://doi.org/10.1086/382040)
- Fletcher, M. T. 2015, Master's thesis, Naval Postgraduate School, Monterey, CA
- Gaensler, B. M., Haverkorn, M., Staveley-Smith, L., et al. 2005, *Science*, 307, 1610, doi: [10.1126/science.1108832](https://doi.org/10.1126/science.1108832)
- Galtier, S., Nazarenko, S. V., Newell, A. C., & Pouquet, A. 2000, *Journal of Plasma Physics*, 63, 447, doi: [10.1017/S0022377899008284](https://doi.org/10.1017/S0022377899008284)
- Goldreich, P., & Kylafis, N. D. 1981, *ApJL*, 243, L75, doi: [10.1086/183446](https://doi.org/10.1086/183446)
- Goldreich, P., & Sridhar, S. 1995, *ApJ*, 438, 763, doi: [10.1086/175121](https://doi.org/10.1086/175121)
- González-Casanova, D. F., & Lazarian, A. 2017, *ApJ*, 835, 41, doi: [10.3847/1538-4357/835/1/41](https://doi.org/10.3847/1538-4357/835/1/41)
- Ho, K. W. 2022, *MHDFlows.jl*, 0.2.1b, Zenodo, doi: [10.5281/zenodo.8242702](https://doi.org/10.5281/zenodo.8242702)
- Ho, K. W., & Lazarian, A. 2023, *MNRAS*, 520, 3857, doi: [10.1093/mnras/stad186](https://doi.org/10.1093/mnras/stad186)
- Ho, K. W., Yuen, K. H., Leung, P. K., & Lazarian, A. 2019, *ApJ*, 887, 258, doi: [10.3847/1538-4357/ab578c](https://doi.org/10.3847/1538-4357/ab578c)
- Hoang, T. 2019, arXiv e-prints, arXiv:1910.12205, doi: [10.48550/arXiv.1910.12205](https://doi.org/10.48550/arXiv.1910.12205)
- Hu, Y., & Lazarian, A. 2022, arXiv e-prints, arXiv:2208.06074, doi: [10.48550/arXiv.2208.06074](https://doi.org/10.48550/arXiv.2208.06074)
- Hu, Y., Lazarian, A., Beck, R., & Xu, S. 2022, *ApJ*, 941, 92, doi: [10.3847/1538-4357/ac9df0](https://doi.org/10.3847/1538-4357/ac9df0)
- Hu, Y., Lazarian, A., Li, Y., Zhuravleva, I., & Gendron-Marsolais, M.-L. 2020a, *ApJ*, 901, 162, doi: [10.3847/1538-4357/abb1c3](https://doi.org/10.3847/1538-4357/abb1c3)
- . 2020b, *ApJ*, 901, 162, doi: [10.3847/1538-4357/abb1c3](https://doi.org/10.3847/1538-4357/abb1c3)
- Hu, Y., Stuardi, C., Lazarian, A., et al. 2024, *Nature Communications*, 15, 1006, doi: [10.1038/s41467-024-45164-8](https://doi.org/10.1038/s41467-024-45164-8)
- Hu, Y., Xu, S., & Lazarian, A. 2021, *ApJ*, 911, 37, doi: [10.3847/1538-4357/abea18](https://doi.org/10.3847/1538-4357/abea18)
- Hu, Y., Yuen, K. H., & Lazarian, A. 2019, *ApJ*, 886, 17, doi: [10.3847/1538-4357/ab4b5e](https://doi.org/10.3847/1538-4357/ab4b5e)
- Hunter, J. D. 2007, *Computing in Science and Engineering*, 9, 90, doi: [10.1109/MCSE.2007.55](https://doi.org/10.1109/MCSE.2007.55)
- Jokipii, J. R. 1966, *ApJ*, 146, 480, doi: [10.1086/148912](https://doi.org/10.1086/148912)
- Knowles, K., Cotton, W. D., Rudnick, L., et al. 2022, *A&A*, 657, A56, doi: [10.1051/0004-6361/202141488](https://doi.org/10.1051/0004-6361/202141488)
- Kraichnan, R. H. 1965, *Physics of Fluids*, 8, 1385, doi: [10.1063/1.1761412](https://doi.org/10.1063/1.1761412)
- Lazarian, A. 2006, *Astronomische Nachrichten*, 327, 609, doi: [10.1002/asna.200610603](https://doi.org/10.1002/asna.200610603)
- . 2007, *Journal of Quantitative Spectroscopy and Radiative Transfer*, 106, 225, doi: [10.1016/j.jqsrt.2007.01.038](https://doi.org/10.1016/j.jqsrt.2007.01.038)
- Lazarian, A., & Hoang, T. 2007, *MNRAS*, 378, 910, doi: [10.1111/j.1365-2966.2007.11817.x](https://doi.org/10.1111/j.1365-2966.2007.11817.x)
- . 2021, *ApJ*, 908, 12, doi: [10.3847/1538-4357/abd02c](https://doi.org/10.3847/1538-4357/abd02c)
- Lazarian, A., & Pogosyan, D. 2012, *ApJ*, 747, 5, doi: [10.1088/0004-637X/747/1/5](https://doi.org/10.1088/0004-637X/747/1/5)
- . 2016, *ApJ*, 818, 178, doi: [10.3847/0004-637X/818/2/178](https://doi.org/10.3847/0004-637X/818/2/178)
- Lazarian, A., & Vishniac, E. T. 1999, *ApJ*, 517, 700, doi: [10.1086/307233](https://doi.org/10.1086/307233)
- Lazarian, A., & Yuen, K. H. 2018a, *ApJ*, 865, 59, doi: [10.3847/1538-4357/aad3ca](https://doi.org/10.3847/1538-4357/aad3ca)
- . 2018b, *ApJ*, 853, 96, doi: [10.3847/1538-4357/aaa241](https://doi.org/10.3847/1538-4357/aaa241)
- Lazarian, A., Yuen, K. H., Lee, H., & Cho, J. 2017, *ApJ*, 842, 30, doi: [10.3847/1538-4357/aa74c6](https://doi.org/10.3847/1538-4357/aa74c6)
- Lithwick, Y., & Goldreich, P. 2001, *ApJ*, 562, 279, doi: [10.1086/323470](https://doi.org/10.1086/323470)
- Mac Low, M.-M., & Klessen, R. S. 2004, *Reviews of Modern Physics*, 76, 125, doi: [10.1103/RevModPhys.76.125](https://doi.org/10.1103/RevModPhys.76.125)
- Maron, J., & Goldreich, P. 2001, *ApJ*, 554, 1175, doi: [10.1086/321413](https://doi.org/10.1086/321413)
- McKee, C. F., & Ostriker, E. C. 2007, *ARA&A*, 45, 565, doi: [10.1146/annurev.astro.45.051806.110602](https://doi.org/10.1146/annurev.astro.45.051806.110602)
- Pakmor, R., van de Voort, F., Bieri, R., et al. 2020, *MNRAS*, 498, 3125, doi: [10.1093/mnras/staa2530](https://doi.org/10.1093/mnras/staa2530)
- Stone, J. M., Tomida, K., White, C. J., & Felker, K. G. 2020, *ApJS*, 249, 4, doi: [10.3847/1538-4365/ab929b](https://doi.org/10.3847/1538-4365/ab929b)
- Tram, L. N., & Hoang, T. 2022, *Frontiers in Astronomy and Space Sciences*, 9, 923927, doi: [10.3389/fspas.2022.923927](https://doi.org/10.3389/fspas.2022.923927)
- Vogt, C., & Enßlin, T. A. 2003, *A&A*, 412, 373, doi: [10.1051/0004-6361:20031434](https://doi.org/10.1051/0004-6361:20031434)
- Xu, S., & Lazarian, A. 2016, *ApJ*, 833, 215, doi: [10.3847/1538-4357/833/2/215](https://doi.org/10.3847/1538-4357/833/2/215)
- Yan, H., & Lazarian, A. 2002, *Physical Review Letters*, 89, B1102+, doi: [10.1103/PhysRevLett.89.281102](https://doi.org/10.1103/PhysRevLett.89.281102)
- . 2006, *ApJ*, 653, 1292, doi: [10.1086/508704](https://doi.org/10.1086/508704)
- . 2008, *ApJ*, 673, 942, doi: [10.1086/524771](https://doi.org/10.1086/524771)
- . 2010, *Highlights of Astronomy*, 15, 446, doi: [10.1017/S1743921310010215](https://doi.org/10.1017/S1743921310010215)
- Yuen, K. H., & Lazarian, A. 2017, *ApJL*, 837, L24, doi: [10.3847/2041-8213/aa6255](https://doi.org/10.3847/2041-8213/aa6255)
- Zhang, J.-F., Hu, K., Cho, J., & Lazarian, A. 2020, *ApJ*, 895, 20, doi: [10.3847/1538-4357/ab88ac](https://doi.org/10.3847/1538-4357/ab88ac)

Zhang, J.-F., Lazarian, A., Ho, K. W., et al. 2019, MNRAS, 486,
4813, doi: [10.1093/mnras/stz1176](https://doi.org/10.1093/mnras/stz1176)

APPENDIX

Table 3. List of Acronyms

Acronym	Definition
AM	Aligment Measrure
SIG	Synchrotron Intensity Gradients
GT	Gradient Techinque
ICM	Intracluster Medium
ISM	Interstellar Medium
LOS	Line of Sight (z)
MHD	Magnetohydrodynamic
POS	Plane of Sky (x-y)
GS95	Goldreich & Sridhar (1995)
LV99	Lazarian & Vishniac (1999)